Supplement of The Cryosphere, 17, 1003–1022, 2023
https://doi.org/10.5194/tc-17-1003-2023-supplement


The Cryosphere Open Access EGU

*Supplement of*

# Grounding line retreat and tide-modulated ocean channels at Moscow University and Totten Glacier ice shelves, East Antarctica

**Tian Li et al.**

*Correspondence to:* Tian Li (tian.li@bristol.ac.uk) and Jonathan L. Bamber (j.bamber@bristol.ac.uk)

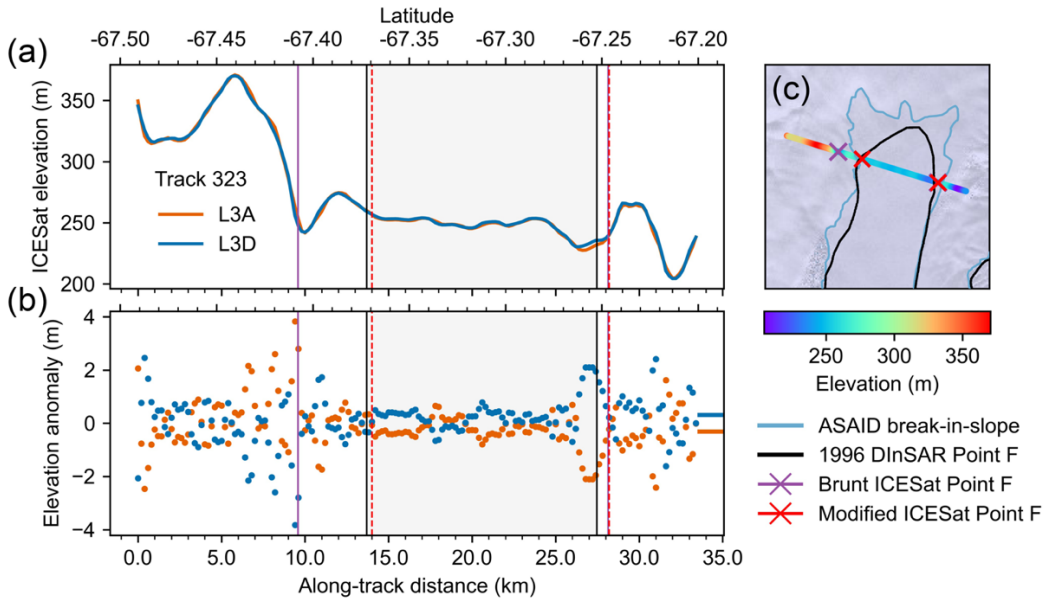


Figure S1. The ICESat-derived elevations (a) and elevation anomalies (b) along the RGT 323 at the main glacier trunk of the Moscow University Ice Shelf (MUIS) (c) processed in this study. The grey zones in (a) and (b) are the 1996 MEaSUREs DInSAR-derived ice shelf (Rignot et al., 2016, 2011). In subplots (a) and (b), the purple solid vertical lines are the Brunt et al. (2011) ICESat-derived Point F, the red dashed vertical lines are the manually picked Point F based on the elevation anomalies from repeat tracks L3A (June 21 – November 8, 2004) and L3D (June 23 – November 24, 2005) in (b). In (c), the data are overlaid on the Landsat Image Mosaic of Antarctica (Bindschadler et al., 2008).

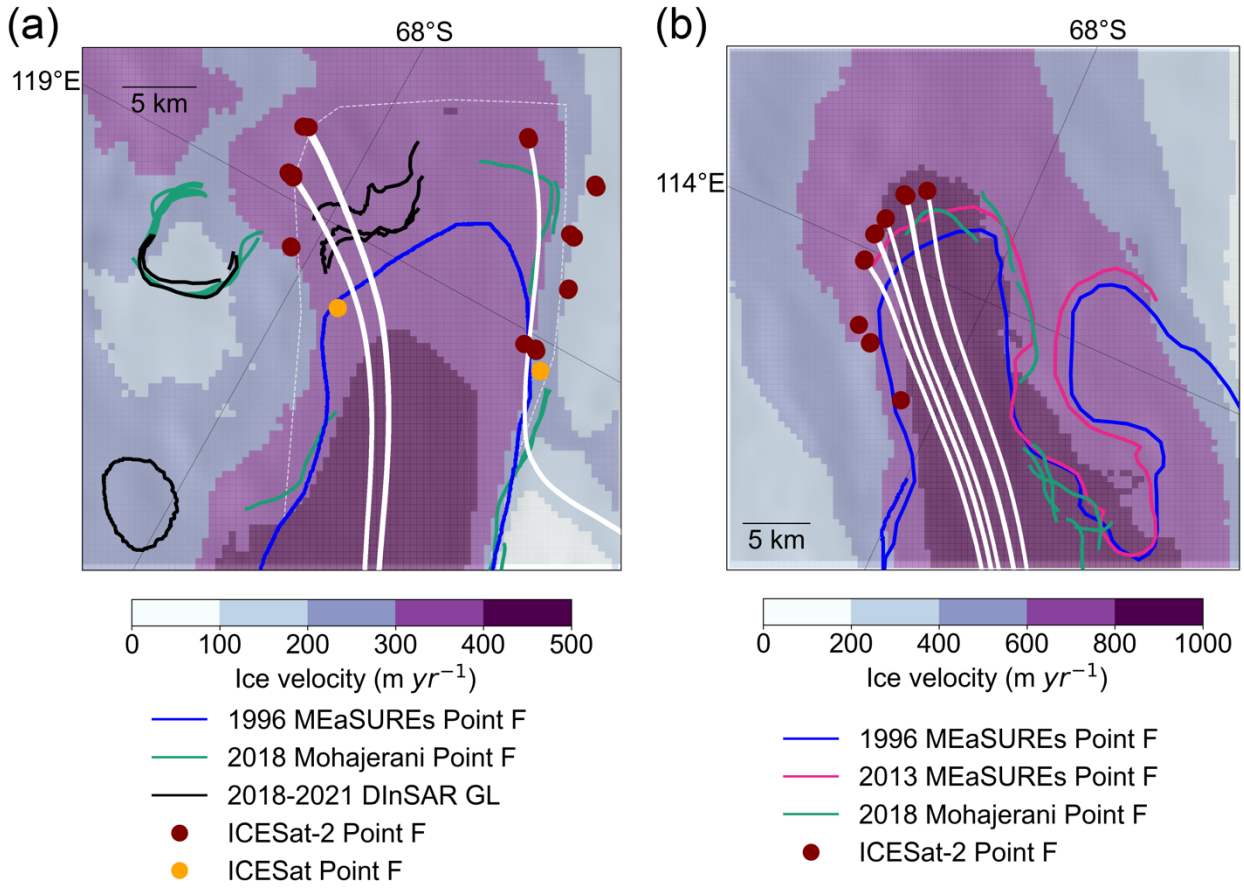

Figure S2. The ice flowlines (white solid lines) used to measure the grounding line migrations between different time stamps at the main glacier trunks for Moscow University Ice Shelf (a) and the Totten Glacier Ice Shelf (b).

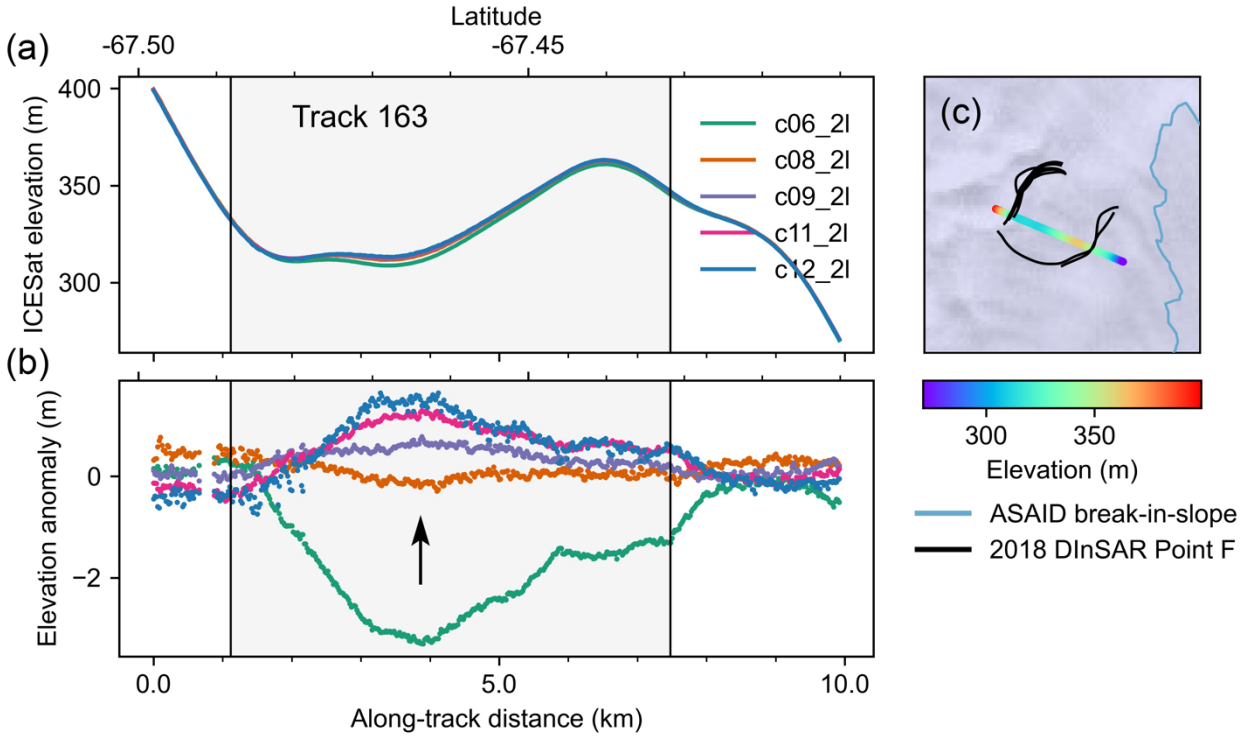


Figure S3. The ICESat-2-derived elevations (a) and elevation anomalies (b) along the track 163 GT2L across the Moscow University Ice Shelf (MUIS) southern subglacial lake (c). The grey zones in (a) and (b) are the subglacial lake boundary from 2018 Sentinel-1a/b DInSAR grounding line product (Mohajerani et al., 2021). In (c), the data are overlaid on the Landsat Image Mosaic of Antarctica (Bindschadler et al., 2008). The ICESat-2 data used in detecting subglacial lake is version 5 between 30 March 2019 and 22 December 2021.

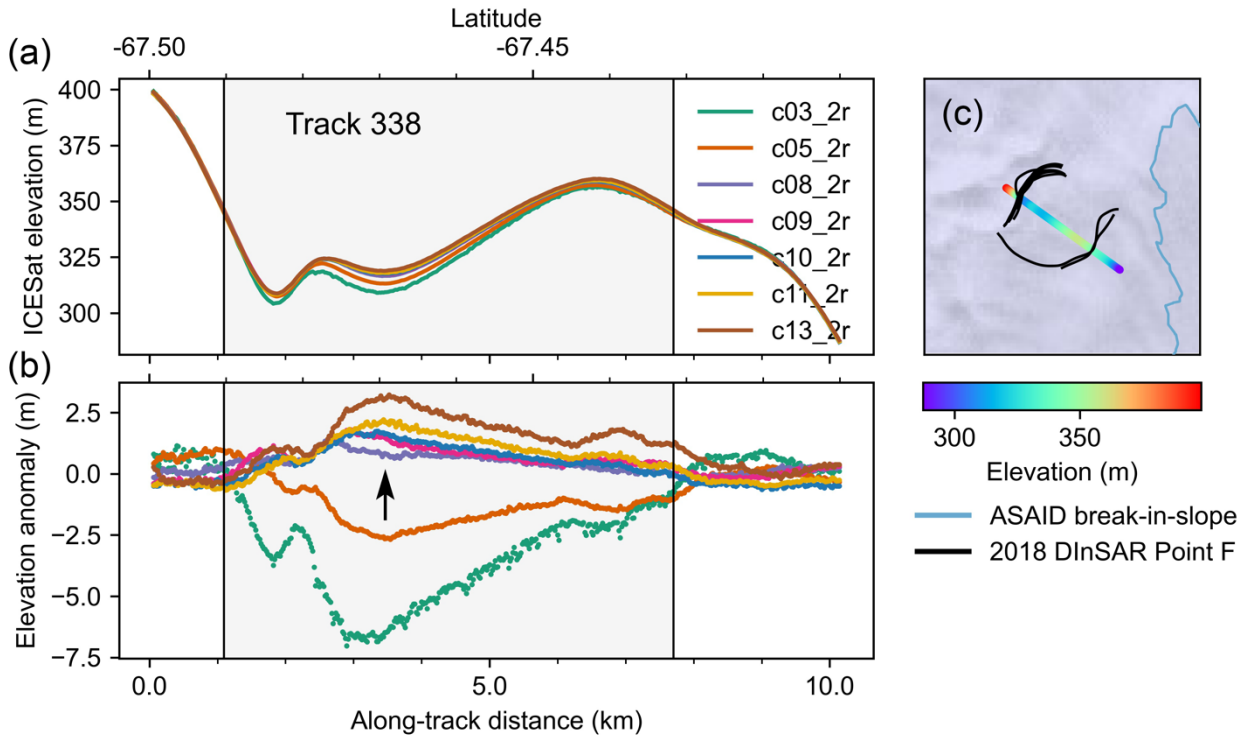

Figure S4. The ICESat-2-derived elevations (a) and elevation anomalies (b) along the track 338 GT2R across the Moscow University Ice Shelf (MUIS) southern subglacial lake (c). The grey zones in (a) and (b) are the subglacial lake boundary from 2018 Sentinel-1a/b DInSAR grounding line product (Mohajerani et al., 2021). In (c), the data are overlaid on the Landsat Image Mosaic of Antarctica (Bindschadler et al., 2008). The ICESat-2 data used in detecting subglacial lake is version 5 between 30 March 2019 and 22 December 2021.

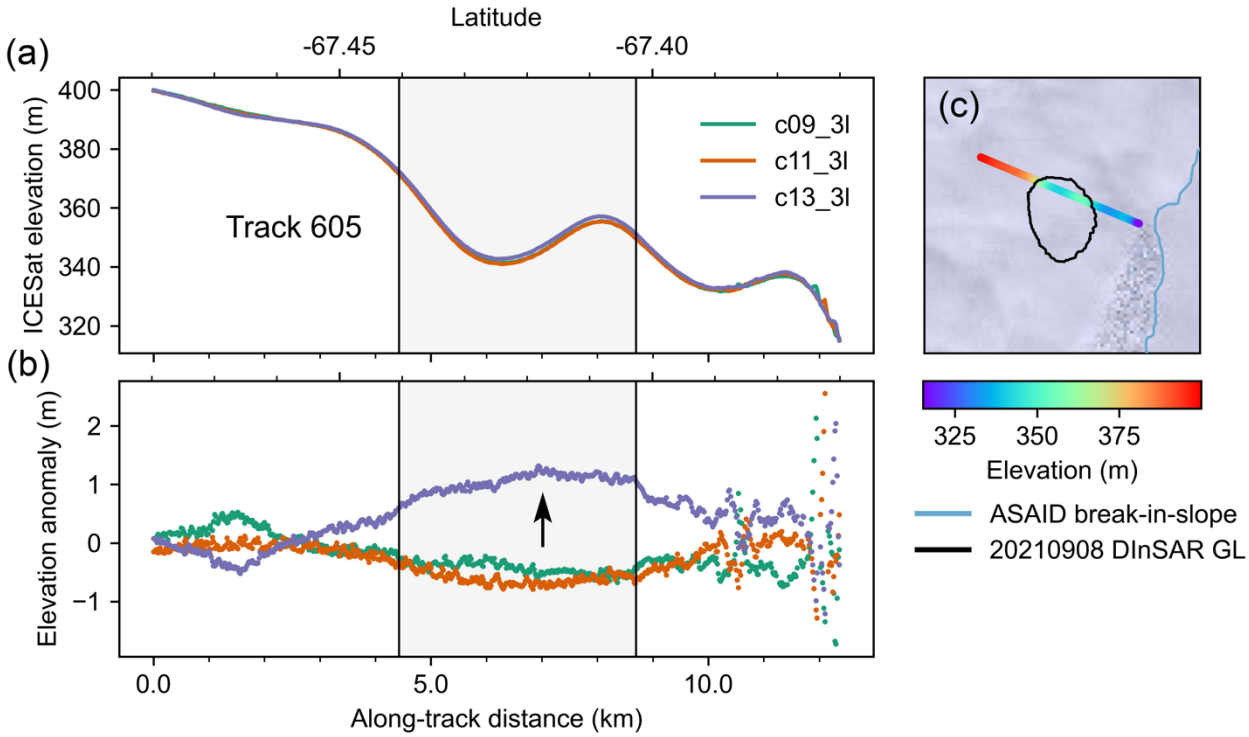


Figure S5. The ICESat-2-derived elevations (a) and elevation anomalies (b) along the track 605 GT3L across the Moscow University Ice Shelf (MUIS) northern subglacial lake (c). The grey zones in (a) and (b) are the subglacial lake boundary from Sentinel-1a/b DInSAR grounding line on 8 September 2021 mapped in this study (Figure 2g). In (c), the data are overlaid on the Landsat Image Mosaic of Antarctica (Bindschadler et al., 2008). The ICESat-2 data used in detecting subglacial lake is version 5 between 30 March 2019 and 22 December 2021.

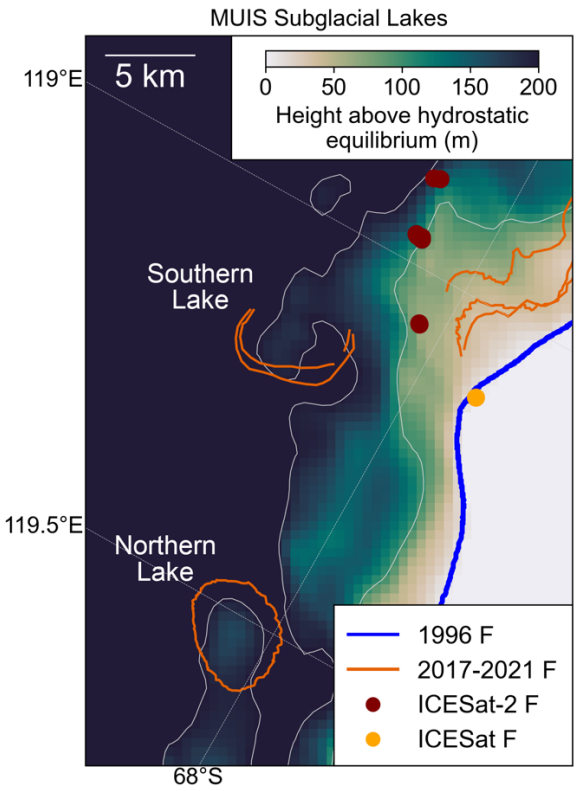


Figure S6. Height above hydrostatic equilibrium at the two subglacial lakes near Moscow University Ice Shelf (MUIS) main glacier trunk mapped in this study (Figure 2).

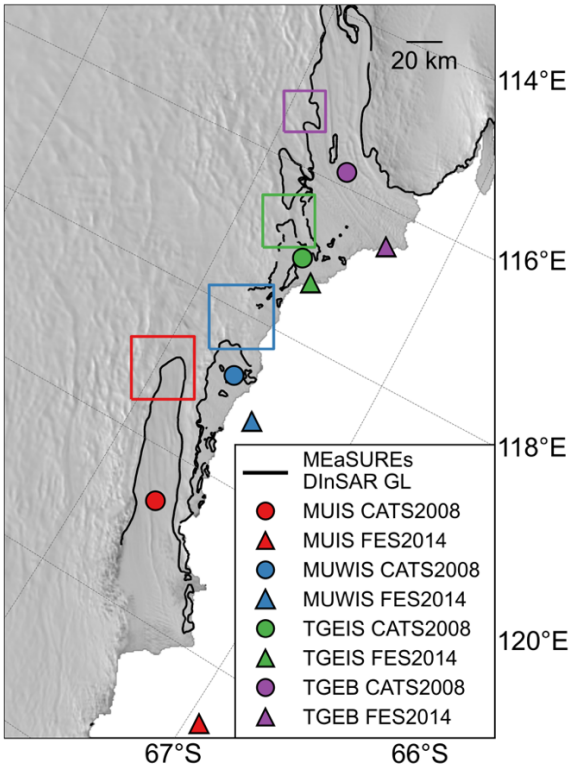


Figure S7. The spatial distributions of the CATS2008 reference points (circles) and FES2014 references points (triangles) used in the DInSAR tidal amplitude predictions for each studied region. Note FES2014 tidal model does not provide tidal predictions over the ice shelves, its tidal prediction reference points are located off coast.

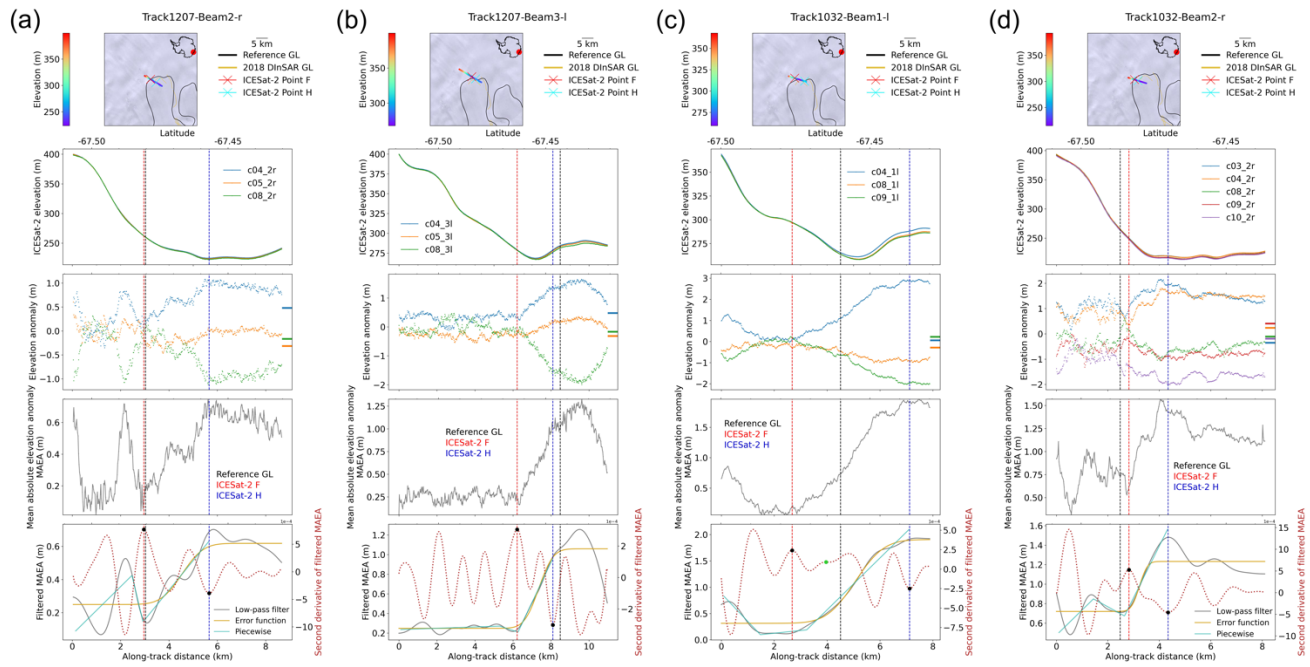


Figure S8. The repeat track analysis of ICESat-2 elevation profiles on the Totten Glacier Ice Shelf (TGIS) main glacier trunk along track 1207 GT2R (a), track 1207 GT3L (b), track 1032 GT1L (c) and track 1032 GT2R (d), respectively.

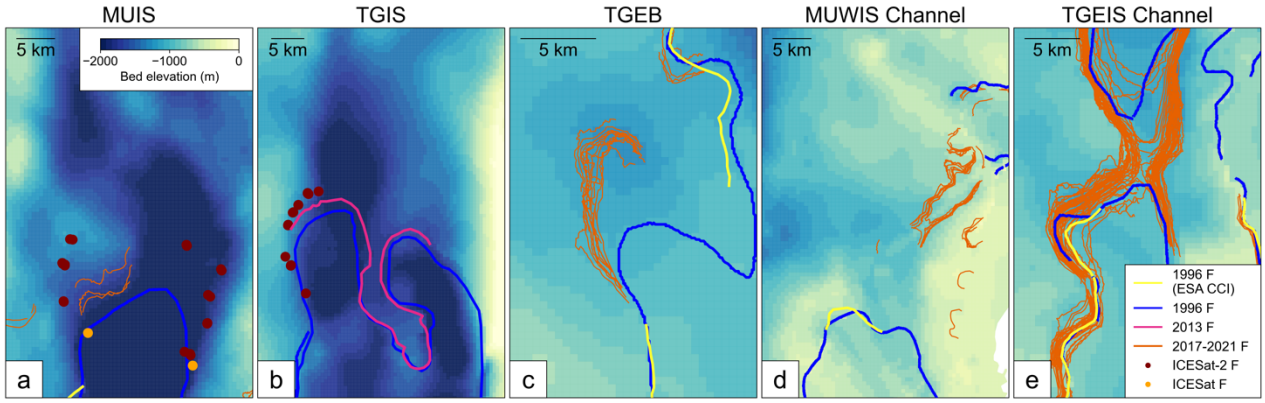


Figure S9. BedMachine bed elevation (Morlighem et al., 2020) overlaid with different grounding zone products. The ESA CCI DInSAR grounding lines in 1996 are shown as the yellow solid lines in all subplots (ESA, 2017).

Table S1. Modelled tidal amplitudes and grounding line (GL) retreat compared with 1996 MEaSUREs GL for Sentinel-1a/b interferograms at Moscow University Ice Shelf (MUIS) main glacier trunk (Fig. 2b). Each row represents a different interferogram generated from three different Sentinel-1 image scenes acquired at time stamps of t1, t2 and t3. The nominal time stamp of each interferogram is t2. h1, h2 and h3 are the tidal amplitude predictions at each acquisition date calculated from CATS2008 (Padman et al., 2002) and FES2014 tidal models (Lyard et al., 2021). The tidal prediction reference points are shown in Figure S7. The tidal amplitudes are used to identify $h_{max}$, the highest positive tides among all different tides ($h_{max}$= max($h_1$, $h_2$, $h_3$)) (Brancato et al., 2020). The differential tidal prediction $\delta h$ from the tidal models for each Sentinel-1a/b DInSAR interferogram is calculated as $\delta h = (h3 - h2) - (h2 - h1)$.

| Time stamp of SAR pass 1 (t1) | Time stamp of SAR pass 2 (t2) | Time stamp of SAR pass 3 (t3) | Modelled tide amplitude h1 at t1 (cm) | Modelled tide amplitude h2 at t2 (cm) | Modelled tide amplitude h3 at t3 (cm) | $h_{max}$ (cm) | $\delta h$ (cm) | GL retreat since 1996 along ice flowline in Figure 2 (km) |
|---|---|---|---|---|---|---|---|---|

| | | | | | | | | |
|---|---|---|---|---|---|---|---|---|
| CATS2008 Tide Model (-67.0714°S, 120.6249°E) | | | | | | | | |
| 20210417T121114 | 20210423T121156 | 20210429T121114 | -27.95 | 34.80 | -80.60 | 34.80 | -178.15 | 3.14 ± 0.13 |
| 20210423T121156 | 20210429T121114 | 20210505T121156 | 34.80 | -80.60 | 32.45 | 34.80 | 228.45 | 5.67 ± 0.13 |
| 20210429T121114 | 20210505T121156 | 20210511T121115 | -80.60 | 32.45 | -50.80 | 32.45 | -196.30 | 3.84 ± 0.13 |
| FES2014 Tide Model (-66.3102°S, 122.6998°E) | | | | | | | | |
| 20210417T121114 | 20210423T121156 | 20210429T121114 | -28.71 | 35.42 | -75.53 | 35.42 | -175.08 | 3.14 ± 0.13 |
| 20210423T121156 | 20210429T121114 | 20210505T121156 | 35.42 | -75.53 | 33.79 | 35.42 | 220.28 | 5.67 ± 0.13 |
| 20210429T121114 | 20210505T121156 | 20210511T121115 | -75.53 | 33.79 | -44.66 | 33.79 | -187.78 | 3.84 ± 0.13 |

Table S2. The acquisition time of ERS-1/2 SAR images used in 1996 MEaSUREs DInSAR grounding line mapping and the corresponding modelled tidal amplitudes calculated from CATS2008 (Padman et al., 2002) and FES2014 tidal models (Lyard et al., 2021) on the Moscow University Western Ice Shelf (MUWIS), Moscow University Ice Shelf (MUIS), Totten Glacier Eastern Ice Shelf (TGEIS), Totten Glacier Ice Shelf (TGIS) and Totten Glacier Eastern Branch (TGEB). The differential tidal predictions $\delta h$ at four satellite passes used in DInSAR interferogram mapping is calculated as $\delta h = (h4 - h3) - (h2 - h1)$ where h1, h2, h3, h4 are the modelled tidal amplitudes at each time stamp (Fricker et al., 2009).

| Time of SAR pass | Latitude | Longitude | CATS2008 tide amplitude (cm) | FES2014 tide amplitude (cm) | CATS2008 $\delta h$ (cm) | FES2014 $\delta h$ (cm) | CATS2008 $\lvert\delta h\rvert$ (cm) | FES2014 $\lvert\delta h\rvert$ (cm) |
|---|---|---|---|---|---|---|---|---|
| MUWIS & MUIS | | | | | | | | |
| 19960214T003648 | -66.3102 | 122.6998 | -34.51 | -38.25 | -11.22 | -10.76 | 11.22 | 10.76 |
| 19960215T003651 | -66.3102 | 122.6998 | -31.01 | -35.28 | | | | |
| 19960320T003651 | -66.3102 | 122.6998 | -18.79 | -21.90 | | | | |
| 19960321T003650 | -66.3102 | 122.6998 | -26.51 | -29.69 | | | | |
| TGEIS | | | | | | | | |
| 19960310T005108 | -66.9212 | 117.2723 | -44.66 | -47.27 | 8.60 | 9.77 | 8.60 | 9.77 |
| 19960311T005107 | -66.9212 | 117.2723 | -45.44 | -47.68 | | | | |
| 19960414T005110 | -66.9212 | 117.2723 | 3.71 | 2.00 | | | | |
| 19960415T005109 | -66.9212 | 117.2723 | 11.53 | 11.36 | | | | |
| TGIS | | | | | | | | |
| 19960313T005654 | -66.6687 | 116.4448 | -38.60 | -41.91 | -15.24 | -14.53 | 15.24 | 14.53 |
| 19960314T005700 | -66.6687 | 116.4448 | -31.45 | -36.09 | | | | |
| 19960417T005658 | -66.6687 | 116.4448 | 10.08 | 10.92 | | | | |
| 19960418T005712 | -66.6687 | 116.4448 | 1.99 | 2.21 | | | | |
| TGEB | | | | | | | | |
| 19960313T005654 | -66.6687 | 116.4448 | -38.60 | -41.91 | -15.35 | -14.64 | 15.35 | 14.64 |
| 19960314T005659 | -66.6687 | 116.4448 | -31.45 | -36.09 | | | | |
| 19960417T005658 | -66.6687 | 116.4448 | 10.08 | 10.92 | | | | |
| 19960418T005657 | -66.6687 | 116.4448 | 1.89 | 2.10 | | | | |

Table S3. The grounding line migration between ICESat-2-derived Point F and MEaSUREs 1996 DInSAR grounding line (GL) along the ice flowlines shown in Figure S2a on the Moscow University Ice Shelf. The tidal ranges are derived from the ICESat-2 elevation anomaly profiles. The time stamp of ICESat-2-derived Point F is defined as year 2020.

| Moscow University Ice Shelf |
|---|

| Track number | GL retreat 1996 - 2020 (km) | GL retreat rate 1996 - 2020 (km $yr^{-1}$) | Tidal range (m) | Ice velocity at Point F (m $yr^{-1}$) | Repeat cycles |
|---|---|---|---|---|---|
| Western flank | | | | | |
| 841-1-l | 13.79 ± 0.1 | 0.57 | 0.89 | 337.5 | 5, 7 |
| 841-1-r | 13.91 ± 0.1 | 0.58 | 0.94 | 337.5 | 5, 7 |
| Eastern flank | | | | | |
| 1108-2-l | 10.95 ± 0.1 | 0.46 | 0.55 | 336.2 | 6, 7 |
| 1108-2-r | 11.13 ± 0.1 | 0.46 | 0.54 | 336.2 | 6, 7 |
| 1283-1-r | 8.71 ± 0.1 | 0.36 | 0.65 | 330.2 | 4, 5 |
| 1108-3-pair | 8.70 ± 0.1 | 0.36 | 0.23 | 329.6 | 6, 7 |
| 1108-3-r | 8.62 ± 0.1 | 0.36 | 0.49 | 329.6 | 6, 7 |
| 1108-3-l | 8.89 ± 0.1 | 0.37 | 0.27 | 330.2 | 6, 7 |
| 1283-1-pair | 9.03 ± 0.1 | 0.38 | 0.61 | 335.1 | 4, 5 |
| 1283-1-l | 8.93 ± 0.1 | 0.37 | 0.61 | 335.1 | 4, 5 |

Table S4. The grounding line migration between ICESat-2-derived Point F and MEaSUREs 1996 DInSAR-derived GL along the ice flowlines shown in Figure S2b at the main glacier trunk of Totten Glacier Ice Shelf (TGIS). The tidal ranges are derived from the ICESat-2 elevation anomalies at Point H. The time stamp of ICESat-2-derived Point F is defined as year 2020.

| Totten Glacier Ice Shelf | | | | | | | |
|---|---|---|---|---|---|---|---|
| Track number | GL retreat 1996 - 2013 (km) | GL retreat 2013 - 2020 (km) | GL retreat rate 2013 - 2020 (km $yr^{-1}$) | GL retreat rate 1996 - 2013 (km $yr^{-1}$) | Tidal Range (m) | Ice velocity at Point F (m $yr^{-1}$) | Repeat cycles |
| 1207-3-l | 2.08 ± 0.1 | 1.64 ± 0.1 | 0.23 | 0.12 | 2.85 | 828.8 | 4, 5, 8 |
| 1032-1-r | 1.97 ± 0.1 | 2.08 ± 0.1 | 0.30 | 0.12 | 4.89 | 820.7 | 4, 8, 9 |
| 1032-1-l | 1.93 ± 0.1 | 2.33 ± 0.1 | 0.33 | 0.11 | 4.86 | 811.7 | 4, 8, 9 |
| 1032-1-pair | 1.93 ± 0.1 | 2.27 ± 0.1 | 0.32 | 0.11 | 4.91 | 811.7 | 4, 8, 9 |
| 1207-2-r | 2.17 ± 0.1 | 1.45 ± 0.1 | 0.21 | 0.13 | 1.98 | 805.2 | 4, 5, 8 |
| 1207-2-pair | 2.16 ± 0.1 | 1.41 ± 0.1 | 0.20 | 0.13 | 2.11 | 805.2 | 4, 5, 8 |
| 1032-2-l | 2.04 ± 0.1 | 1.37 ± 0.1 | 0.20 | 0.12 | 3.86 | 753.9 | 3,4,8,9,10 |
| 1032-2-pair | 2.03 ± 0.1 | 1.38 ± 0.1 | 0.20 | 0.12 | 3.96 | 753.9 | 3,4,8,9,10 |
| 1032-2-r | 2.02 ± 0.1 | 1.40 ± 0.1 | 0.20 | 0.12 | 3.92 | 753.9 | 3,4,8,9,10 |
| 1207-1-r | 2.03 ± 0.1 | 0.81 ± 0.1 | 0.12 | 0.12 | 0.83 | 715.8 | 4, 5 |
| 1207-1-l | 2.05 ± 0.1 | 0.77 ± 0.1 | 0.11 | 0.12 | 1.06 | 715.8 | 4, 5 |
| 1207-1-pair | 2.04 ± 0.1 | 0.75 ± 0.1 | 0.11 | 0.12 | 1.09 | 715.8 | 4, 5 |

Table S5. Modelled tidal amplitudes and grounding line (GL) retreat compared with 1996 MEaSUREs GL for Sentinel-1a/b interferograms at the Totten Glacier East Branch (TGEB) ice stream (Fig. 6). Each row represents a different interferogram generated from three different Sentinel-1 image scenes acquired at time stamps of t1, t2 and t3. The nominal time stamp of each interferogram is t2. h1, h2 and h3 are the tidal amplitude predictions at each acquisition date calculated from CATS2008 (Padman et al., 2002) and FES2014 tidal models (Lyard et al., 2021). The tidal prediction reference points are shown in Figure S7. The tidal amplitudes are used to identify $h_{max}$, the highest tidal amplitude ($h_{max}=\max(h_1, h_2, h_3)$) (Brancato et al., 2020). The differential tidal prediction δh from the tidal models for each Sentinel-1a/b DInSAR interferogram is calculated as $\delta h = (h3 - h2) - (h2 - h1)$.

| Time stamp of SAR pass 1 (t1) | Time stamp of SAR pass 2 (t2) | Time stamp of SAR pass 3 (t3) | Modelled tide amplitude h1 at t1 (cm) | Modelled tide amplitude h2 at t2 (cm) | Modelled tide amplitude h3 at t3 (cm) | $h_{max}$ (cm) | δh (cm) | GL retreat since 1996 along ice flowline in Figure 6 (km) |
|---|---|---|---|---|---|---|---|---|
| CATS2008 Tidal Model (-67.0043°S, 115.8222°E) | | | | | | | | |
| 20180301T123555 | 20180307T123513 | 20180313T123556 | -2.64 | -23.07 | 34.82 | 34.82 | 78.31 | 5.15 ± 0.13 |
| 20190119T123603 | 20190125T123521 | 20190131T123602 | 62.07 | -51.09 | 50.53 | 62.07 | 214.77 | 4.84 ± 0.13 |
| 20190302T123520 | 20190308T123602 | 20190314T123520 | 40.04 | -47.65 | 12.88 | 40.04 | 148.21 | 6.57 ± 0.13 |
| 20190308T123602 | 20190314T123520 | 20190320T123602 | -47.65 | 12.88 | -14.5 | 12.88 | -87.9 | 6.45 ± 0.13 |
| 20190507T123603 | 20190513T123522 | 20190519T123604 | -67.43 | 31.79 | -67.92 | 31.79 | -198.93 | 6.96 ± 0.13 |
| 20200308T123526 | 20200314T123608 | 20200320T123527 | 21.77 | -36.85 | 32.65 | 32.65 | 128.13 | 4.64 ± 0.13 |
| 20200401T123527 | 20200407T123609 | 20200413T123527 | 15.07 | -28.61 | -9.58 | 15.07 | 62.71 | 6.76 ± 0.13 |
| 20200718T123532 | 20200724T123615 | 20200730T123533 | -40 | -47 | -29.78 | -29.78 | 24.23 | 6.06 ± 0.13 |
| 20210309T123614 | 20210315T123532 | 20210321T123614 | 54.46 | -57.46 | 11.93 | 54.46 | 181.31 | 6.4 ± 0.13 |
| 20210402T123614 | 20210408T123533 | 20210414T123615 | -35.04 | 22.07 | -62.81 | 22.07 | -141.99 | 5.58 ± 0.13 |
| 20210420T123533 | 20210426T123615 | 20210502T123534 | 17.55 | -42.46 | -3.08 | 17.55 | 99.37 | 6 ± 0.13 |
| FES2014 Tidal Model (-66.6687°S, 116.4448°E) | | | | | | | | |
| 20180301T123555 | 20180307T123513 | 20180313T123556 | 3.42 | -20.85 | 38.46 | 38.46 | 83.58 | 5.15 ± 0.13 |
| 20190119T123603 | 20190125T123521 | 20190131T123602 | 66.61 | -48.72 | 55.54 | 66.61 | 219.59 | 4.84 ± 0.13 |
| 20190302T123520 | 20190308T123602 | 20190314T123520 | 43.98 | -43.14 | 15.77 | 43.98 | 146.04 | 6.57 ± 0.13 |
| 20190308T123602 | 20190314T123520 | 20190320T123602 | -43.14 | 15.77 | -7.77 | 15.77 | -82.46 | 6.45 ± 0.13 |
| 20190507T123603 | 20190513T123522 | 20190519T123604 | -65.6 | 32.93 | -66.61 | 32.93 | -198.06 | 6.96 ± 0.13 |
| 20200308T123526 | 20200314T123608 | 20200320T123527 | 28.23 | -34.34 | 36.6 | 36.6 | 133.52 | 4.64 ± 0.13 |
| 20200401T123527 | 20200407T123609 | 20200413T123527 | 17.94 | -23.34 | -7.06 | 17.94 | 57.57 | 6.76 ± 0.13 |
| 20200718T123532 | 20200724T123615 | 20200730T123533 | -42.74 | -47.63 | -31.76 | -31.76 | 20.77 | 6.06 ± 0.13 |
| 20210309T123614 | 20210315T123532 | 20210321T123614 | 60.17 | -52.41 | 13.72 | 60.17 | 178.71 | 6.4 ± 0.13 |
| 20210402T123614 | 20210408T123533 | 20210414T123615 | -32.04 | 27.58 | -58.51 | 27.58 | -145.71 | 5.58 ± 0.13 |
| 20210420T123533 | 20210426T123615 | 20210502T123534 | 21.23 | -38.59 | -0.27 | 21.23 | 98.14 | 6 ± 0.13 |

Table S6. Modelled tidal amplitudes and grounding line (GL) retreat compared with 1996 MEaSUREs GL for Sentinel-1a/b interferograms at the Moscow University Western Ice Shelf (MUWIS) ocean channel (Fig. 8). Each row represents a different interferogram generated from three different Sentinel-1 image scenes acquired at time stamps of t1, t2 and t3. The nominal time stamp of each interferogram is t2. h1, h2 and h3 are the tidal amplitude predictions at each acquisition date calculated from CATS2008 (Padman et al., 2002) and FES2014 tidal models (Lyard et al., 2021). The tidal prediction reference points are shown in Figure S7. The tidal amplitudes are used to identify $h_{max}$, the highest tidal amplitude ($h_{max}$=max($h_1$, $h_2$, $h_3$)) (Brancato et al., 2020). The absolute differential tidal prediction |δh| from the tidal models for each Sentinel-1a/b DInSAR interferogram is calculated as $|\delta h| = |(h3 - h2) - (h2 - h1)|$.

| Time stamp of SAR pass 1 (t1) | Time stamp of SAR pass 2 (t2) | Time stamp of SAR pass 3 (t3) | Modelled tide amplitude h1 at t1 (cm) | Modelled tide amplitude h2 at t2 (cm) | Modelled tide amplitude h3 at t3 (cm) | $h_{max}$ (cm) | \|δh\|(cm) | Channel width (m) |
|---|---|---|---|---|---|---|---|---|
| CATS2008 Tidal Model (-67.0407°S, 118.756°E) | | | | | | | | |
| 20180304T121054 | 20180310T121136 | 20180316T121054 | -61.26 | 29.14 | -10.02 | 29.14 | 129.56 | 3128 ± 127 |
| 20180322T121136 | 20180328T121054 | 20180403T121136 | -35.4 | 34.74 | -58.13 | 34.74 | 163.01 | 1442 ± 127 |
| 20200305T121107 | 20200311T121149 | 20200317T121107 | 56.74 | -71.91 | 43.07 | 56.74 | 243.63 | 2666 ± 127 |
| 20210411T121155 | 20210417T121114 | 20210423T121156 | -38.12 | -24.39 | 32.52 | 32.52 | 43.18 | 0 |
| 20210417T121114 | 20210423T121156 | 20210429T121114 | -24.39 | 32.52 | -77.55 | 32.52 | 166.98 | 2187 ± 127 |
| 20210423T121156 | 20210429T121114 | 20210505T121156 | 32.52 | -77.55 | 32.11 | 32.52 | 219.73 | 2837 ± 127 |
| 20210429T121114 | 20210505T121156 | 20210511T121115 | -77.55 | 32.11 | -51.67 | 32.11 | 193.44 | 1621 ± 127 |
| FES2014 Tidal Model (-66.8536°S, 119.1516°E) | | | | | | | | |
| 20180304T121054 | 20180310T121136 | 20180316T121054 | -60.57 | 30.05 | -7.39 | 30.05 | 128.07 | 3128 ± 127 |
| 20180322T121136 | 20180328T121054 | 20180403T121136 | -33.99 | 39.37 | -57.17 | 39.37 | 169.9 | 1442 ± 127 |
| 20200305T121107 | 20200311T121149 | 20200317T121107 | 58.87 | -70 | 47.38 | 58.87 | 246.25 | 2666 ± 127 |
| 20210411T121155 | 20210417T121114 | 20210423T121156 | -35.19 | -25.68 | 35.3 | 35.3 | 51.47 | 0 |

| | | | | | | | | |
|---|---|---|---|---|---|---|---|---|
| 20210417T121114 | 20210423T121156 | 20210429T121114 | -25.68 | 35.3 | -76.7 | 35.3 | 172.98 | 2187 ± 127 |
| 20210423T121156 | 20210429T121114 | 20210505T121156 | 35.3 | -76.7 | 36.87 | 36.87 | 225.57 | 2837 ± 127 |
| 20210429T121114 | 20210505T121156 | 20210511T121115 | -76.7 | 36.87 | -48.76 | 36.87 | 199.2 | 1621 ± 127 |

Table S7. Modelled tidal amplitudes and grounding line (GL) retreat compared with 1996 MEaSUREs GL for Sentinel-1a/b interferograms at the Totten Glacier Eastern Ice Shelf (TGEIS) ocean channel (Fig. 9). Each row represents a different interferogram generated from three different Sentinel-1 image scenes acquired at time stamps of t1, t2 and t3. The nominal time stamp of each interferogram is t2. h1, h2 and h3 are the tidal amplitude predictions at each acquisition date calculated from CATS2008 (Padman et al., 2002) and FES2014 tidal models (Lyard et al., 2021). The tidal prediction reference points are shown in Figure S7. The tidal amplitudes are used to identify $h_{max}$, the highest tidal amplitude ($h_{max}$=max($h_1$, $h_2$, $h_3$)) (Brancato et al., 2020). The absolute differential tidal prediction |δh| from the tidal models for each Sentinel-1a/b DInSAR interferogram are calculated as $|\delta h| = |(h3 - h2) - (h2 - h1)|$.

| Time stamp of SAR pass 1 (t1) | Time stamp of SAR pass 2 (t2) | Time stamp of SAR pass 3 (t3) | Modelled tide amplitude h1 at t1 (cm) | Modelled tide amplitude h2 at t2 (cm) | Modelled tide amplitude h3 at t3 (cm) | $h_{max}$ (cm) | \|δh\| (cm) | Channel width (m) |
|---|---|---|---|---|---|---|---|---|
| CATS2008 Tidal Model (-67.0131°S, 117.0389°E) | | | | | | | | |
| 20170818T121137 | 20170824T121056 | 20170830T121138 | -30.65 | -49.05 | -24.28 | -24.28 | 43.16 | 0 |
| 20171101T123559 | 20171107T123517 | 20171113T123558 | 12.19 | -36.40 | 10.85 | 12.19 | 95.83 | 2950 ± 127 |
| 20180304T121054 | 20180310T121136 | 20180316T121054 | -62.85 | 29.88 | -12.60 | 29.88 | 135.20 | 3858 ± 127 |
| 20180310T121136 | 20180316T121054 | 20180322T121136 | 29.88 | -12.60 | -34.79 | 29.88 | 20.29 | 0 |
| 20180322T121136 | 20180328T121054 | 20180403T121136 | -34.79 | 33.19 | -59.05 | 33.19 | 160.22 | 1814 ± 127 |
| 20190305T121142 | 20190311T121101 | 20190317T121142 | -5.50 | -39.57 | 58.67 | 58.67 | 132.31 | 1749 ± 127 |
| 20190311T121101 | 20190317T121142 | 20190323T121101 | -39.57 | 58.67 | -73.56 | 58.67 | 230.47 | 3505 ± 127 |
| 20190317T121142 | 20190323T121101 | 20190329T121143 | 58.67 | -73.56 | 34.32 | 58.67 | 240.10 | 3893 ± 127 |
| 20200715T121113 | 20200721T121155 | 20200727T121113 | -16.48 | -59.61 | -16.65 | -16.48 | 86.09 | 0 |
| 20200727T121113 | 20200802T121156 | 20200808T121114 | -16.65 | -51.45 | -31.80 | -16.65 | 54.45 | 1236 ± 127 |
| 20200814T121156 | 20200820T121115 | 20200826T121157 | -30.25 | -56.06 | -32.94 | -30.25 | 48.92 | 1516 ± 127 |
| 20210411T121155 | 20210417T121114 | 20210423T121156 | -40.75 | -24.00 | 31.79 | 31.79 | 39.04 | 0 |
| 20210417T121114 | 20210423T121156 | 20210429T121114 | -24.00 | 31.79 | -78.84 | 31.79 | 166.41 | 2613 ± 127 |
| 20210423T121156 | 20210429T121114 | 20210505T121156 | 31.79 | -78.84 | 32.39 | 32.39 | 221.86 | 2887 ± 127 |
| FES2014 Tidal Model (-66.9212°S, 117.2723°E) | | | | | | | | |
| 20170818T121137 | 20170824T121056 | 20170830T121138 | -34.18 | -51.70 | -27.03 | -27.03 | 42.19 | 0 |
| 20171101T123559 | 20171107T123517 | 20171113T123558 | 10.35 | -35.61 | 12.57 | 12.57 | 94.14 | 2950 ± 127 |
| 20180304T121054 | 20180310T121136 | 20180316T121054 | -61.90 | 31.06 | -9.95 | 31.06 | 133.97 | 3858 ± 127 |
| 20180310T121136 | 20180316T121054 | 20180322T121136 | 31.06 | -9.95 | -32.80 | 31.06 | 18.16 | 0 |
| 20180322T121136 | 20180328T121054 | 20180403T121136 | -32.80 | 38.00 | -57.80 | 38.00 | 166.60 | 1814 ± 127 |
| 20190305T121142 | 20190311T121101 | 20190317T121142 | -2.51 | -39.54 | 62.50 | 62.50 | 139.07 | 1749 ± 127 |
| 20190311T121101 | 20190317T121142 | 20190323T121101 | -39.54 | 62.50 | -72.47 | 62.50 | 237.01 | 3505 ± 127 |
| 20190317T121142 | 20190323T121101 | 20190329T121143 | 62.50 | -72.47 | 36.94 | 62.50 | 244.38 | 3893 ± 127 |
| 20200715T121113 | 20200721T121155 | 20200727T121113 | -16.49 | -59.69 | -17.72 | -16.49 | 85.17 | 0 |
| 20200727T121113 | 20200802T121156 | 20200808T121114 | -17.72 | -53.95 | -33.99 | -17.72 | 56.20 | 1236 ± 127 |
| 20200814T121156 | 20200820T121115 | 20200826T121157 | -33.30 | -56.60 | -34.18 | -33.30 | 45.73 | 1516 ± 127 |
| 20210411T121155 | 20210417T121114 | 20210423T121156 | -37.74 | -24.78 | 34.70 | 34.70 | 46.51 | 0 |
| 20210417T121114 | 20210423T121156 | 20210429T121114 | -24.78 | 34.70 | -77.50 | 34.70 | 171.67 | 2613 ± 127 |
| 20210423T121156 | 20210429T121114 | 20210505T121156 | 34.70 | -77.50 | 37.39 | 37.39 | 227.08 | 2887 ± 127 |

## References


Bindschadler, R., Vornberger, P., Fleming, A., Fox, A., Mullins, J., Binnie, D., Paulsen, S. J., Granneman, B., and Gorodetzky, D.: The Landsat Image Mosaic of Antarctica, Remote Sens. Environ., 112, 4214–4226, https://doi.org/10.1016/J.RSE.2008.07.006, 2008.

Brancato, V., Rignot, E., Milillo, P., Morlighem, M., Mouginot, J., An, L., Scheuchl, B., Jeong, S., Rizzoli, P., Bueso Bello, J. L., and Prats-Iraola, P.: Grounding Line Retreat of Denman Glacier, East Antarctica, Measured With COSMO-SkyMed Radar Interferometry Data, Geophys. Res. Lett., 47, https://doi.org/10.1029/2019GL086291, 2020.

ESA: Antarctic Ice Sheet Climate Change Initiative, Grounding Line Locations for the Denman and Totten Glaciers, Antarctica, 1996–2015 v1.0, Cent. Environ. Data Anal., 2017.

Fricker, H. A., Coleman, R., Padman, L., Scambos, T. A., Bohlander, J., and Brunt, K. M.: Mapping the grounding zone of the Amery Ice Shelf, East Antarctica using InSAR, MODIS and ICESat, Antarct. Sci., https://doi.org/10.1017/S095410200999023X, 2009.

Lyard, F. H., Allain, D. J., Cancet, M., Carrère, L., and Picot, N.: FES2014 global ocean tide atlas: Design and performance, Ocean Sci., 17, 615–649, https://doi.org/10.5194/OS-17-615-2021, 2021.

Mohajerani, Y., Jeong, S., Scheuchl, B., Velicogna, I., Rignot, E., and Milillo, P.: Automatic delineation of glacier grounding lines in differential interferometric synthetic-aperture radar data using deep learning, Sci. Rep., 11, 4992, https://doi.org/10.1038/s41598-021-84309-3, 2021.

Morlighem, M., Rignot, E., Binder, T., Blankenship, D., Drews, R., Eagles, G., Eisen, O., Ferraccioli, F., Forsberg, R., Fretwell, P., Goel, V., Greenbaum, J. S., Gudmundsson, H., Guo, J., Helm, V., Hofstede, C., Howat, I., Humbert, A., Jokat, W., Karlsson, N. B., Lee, W. S., Matsuoka, K., Millan, R., Mouginot, J., Paden, J., Pattyn, F., Roberts, J., Rosier, S., Ruppel, A., Seroussi, H., Smith, E. C., Steinhage, D., Sun, B., Broeke, M. R. va. den, Ommen, T. D. va., Wessem, M. van, and Young, D. A.: Deep glacial troughs and stabilizing ridges unveiled beneath the margins of the Antarctic ice sheet, Nat. Geosci., 13, 132–137, https://doi.org/10.1038/s41561-019-0510-8, 2020.

Padman, L., Fricker, H. A., Coleman, R., Howard, S., and Erofeeva, L.: A new tide model for the Antarctic ice shelves and seas, Ann. Glaciol., 34, 247–254, https://doi.org/10.3189/172756402781817752, 2002.

Rignot, E., Mouginot, J., and Scheuchl, B.: Antarctic grounding line mapping from differential satellite radar interferometry, Geophys. Res. Lett., 38, https://doi.org/10.1029/2011GL047109, 2011.

Rignot, E., Mouginot, J., and Scheuchl, B.: MEaSUREs Antarctic Grounding Line from Differential Satellite Radar Interferometry, Version 2. Boulder, Colorado USA, NASA Natl. Snow Ice Data Cent. Distrib. Act. Arch. Cent., https://doi.org/https://doi.org/10.5067/IKBWW4RYHF1Q, 2016.